mater.scichina.com link.springer.com

Published online 9 August 2022 | https://doi.org/10.1007/s40843-022-2129-1
Sci China Mater 2023, 66(1): 61–68

A novel PbSe@CNTs anode material based on dual conversion-alloying mechanism for sodium-ion batteries

Dongdong Zhao[1], Ning Zhang[1*], Xiaoying Zhao[1], Ningbo Liu[1], Bin Qin[2], Mande Qiu[1] and Liubin Wang[1*]

ABSTRACT Sodium-ion batteries (SIBs) have been regarded as one of the most promising candidates for filling the application vacancy of lithium-ion batteries for large-scale electrical energy storage. However, anodes with high reversible capacities and fast reaction kinetics are lacking and must be investigated. In this study, a composite consisting of PbSe nanoparticles and carbon nanotubes (PbSe@CNTs) was prepared *via* a simple mechanical ball-milling method with the recovered Pb from lead-acid batteries and commercial Se powder. The introduced CNT networks can encompass and segregate PbSe nanoparticles, thus suppressing their aggregation and increasing the electronic conductivity. The nanosized PbSe and anfractuous CNTs benefit the electrolyte penetration, which shortens the diffusion distance of Na^+ and electrons and relieves the strain upon the sodiation/desodiation process, resulting in an improved rate capability and long cycling. Therefore, the PbSe@CNTs electrodes exhibited a high reversible capacity of 597 $mA\,h\,g^{-1}$ at 20 $mA\,g^{-1}$ and 458.9 $mA\,h\,g^{-1}$ for 100 cycles at 100 $mA\,g^{-1}$ with a capacity retention of 88%. The two-step conversion-alloying mechanism of PbSe with Na to form Na_2Se and $Na_{15}Pb_4$ was confirmed by *ex situ* X-ray diffraction and Raman spectroscopy. The results of this study provide valuable guidance for the design and synthesis of high-performance anodes for SIBs.

Keywords: sodium-ion batteries, PbSe, CNTs, conversion-alloying mechanism, energy storage

INTRODUCTION

With the rapid development of society, electrical energy storage systems have become increasingly critical. Sodium-ion batteries (SIBs) have attracted significant attention owing to the abundance and wide distribution of Na resources, which allow them to fill the application vacancy of lithium-ion batteries (LIBs) and make them promising for large-scale electrical energy storage [1–3]. However, because of the larger size of Na^+ (1.02 Å), the classical anode of LIBs cannot work well, which may lead to sluggish kinetics and large volume changes during the charge/discharge process [4,5]. For example, the commercial graphite anode materials in SIBs have low capacities (~35 $mA\,h\,g^{-1}$) and only exhibit ~110 $mA\,h\,g^{-1}$ under co-interaction with a glyme-based solvent [6–9]. Thus, finding high-capacity and high-performance anode materials for SIBs is imperative.

Recently, various high-capacity anode materials (theoretical capacity >400 $mA\,h\,g^{-1}$) have been developed, such as metal oxides, alloys, chalcogenides, and organic materials [10–15]. Among them, metal selenides (M_xSe), which have the merits of high theoretical capacities, abundant resources, and chemical stability, have received constant attention [16–21]. Moreover, as anode materials for SIBs, metal selenides typically exhibit faster kinetics and lower discharge plateaus than their sulfide counterparts [16,22,23]. For example, layered $TiSe_2$ (as a Na-storage electrode) displayed fast Na^+ diffusion (3.21×10^{-11}–1.20×10^{-9} $cm^2\,s^{-1}$) and a discharge capacity of 113.9 $mA\,h\,g^{-1}$ for $NaTiSe_2$ [24]. A Cu_2Se anode with a porous array architecture for SIBs exhibited a discharge capacity of 426 $mA\,h\,g^{-1}$ with the discharge potential below 1.5 V at a current density of 0.1 $A\,g^{-1}$ [25]. A ZnSe/multi-walled carbon nanotubes (MWCNTs) anode prepared by Mai's group [26] exhibited 382 $mA\,h\,g^{-1}$ after 180 cycles, and amorphization occurred after the first Na insertion. Nevertheless, the M sites of M_xSe are usually non-active elements, which reduces the theoretical capacity of metal selenides [27–31]. Introducing an active alloying metal at the M site favors increasing the capacity [32]. Pb is widely used as a negative electrode in lead-acid batteries. When applied as an anode for SIBs, it exhibits a high theoretical capacity of 485 $mA\,h\,g^{-1}$ because of an alloying mechanism by forming $Na_{15}Pb_4$ [33]. Additionally, the recovery of Pb from waste lead-acid batteries will reduce the manufacturing cost and introduce a new market for the waste lead-acid battery industry [34]. Theoretically, alloying Pb and Se to form PbSe can deliver a capacity of 538.7 $mA\,h\,g^{-1}$, owing to the dual conversion-alloying Na-storage mechanism for SIBs [35–38]. Therefore, it brings about great interest to study the Na-storage performance and mechanism of PbSe in SIBs.

In this study, we prepared PbSe nanoparticles surrounded by CNTs (PbSe@CNTs) *via* a simple mechanical ball-milling method with the recovered Pb from waste lead-acid batteries and commercial Se powder. With the winding and buffering of the introduced CNTs, the aggregation of PbSe nanoparticles is avoided, and the particle size of PbSe is reduced. Additionally, the hierarchical conductive network provided by CNTs offers a robust electronic transport path, increasing the electronic conductivity. Thus, PbSe@CNTs electrodes exhibited a high reversible capacity of 597 $mA\,h\,g^{-1}$ at a current density of 20 $mA\,g^{-1}$ and 458.9 $mA\,h\,g^{-1}$ for 100 cycles at a current density of 100 $mA\,g^{-1}$ with a capacity retention of 88%. The good elec-

---

[1] College of Chemistry and Environmental Science, Key Laboratory of Analytical Science and Technology of Hebei Province, Hebei University, Baoding 071002, China

[2] Department of Chemistry, The University of Hong Kong, Pokfulam Road, Hong Kong SAR, China

[*] Corresponding authors (emails: lbwang@hbu.edu.cn (Wang L); ningzhang@hbu.edu.cn (Zhang N))

trochemical performance is attributed to the ultrafine and evenly distributed PbSe nanoparticles and highly conductive CNTs, which enhance the transport dynamics of the PbSe@CNTs for both electrons and ions. Additionally, the nanosized PbSe and anfractuous CNTs efficiently buffered the expansion of Se and Pb during the cycling, thus maintaining the structural integrity of the hybrid composite. Moreover, experimental results indicate that the PbSe material undergoes a reversible Na-storage reaction of $PbSe + 5.75Na^+ + 5.75e^- \leftrightarrow 0.25Na_{15}Pb_4 + Na_2Se$ during the sodiation/desodiation process. This study provides valuable guidance for the design and synthesis of dual conversion-alloying anodes for high-capacity SIBs.

EXPERIMENTAL SECTION

Material preparation

Pb powder was obtained and recycled from waste lead-acid batteries using a self-developed recycling method in our laboratory. Se powder was purchased from Beijing InnoChem Science & Technology Co., Ltd. PbSe@CNTs composites were synthesized *via* high-energy mechanical ball milling (Fritsch mill -7, Germany). Pb and Se powders with a stoichiometric ratio of 1:1 were mixed with 10 wt% CNTs, followed by manual grinding in a mortar for 10 min under an Ar atmosphere to achieve uniform mixing. Then, the mixtures were transferred to a ball-mill tank containing steel balls. The PbSe@CNTs composites were obtained after 10-h ball milling at a speed of 400 r min^{-1}. The PbSe nanoparticles were prepared *via* the same method but without the addition of CNTs.

Material characterizations

X-ray diffraction (XRD) patterns were recorded by a Bruker D8 Advance diffractometer with Cu Kα radiation in the 2θ range of 5°–80° at a sweep rate of 4° min^{-1}. The morphology of the samples was examined using a JEOL JSM-7500F field-emission scanning electron microscope (FESEM). Transmission electron microscopy (TEM) images were obtained using an FEI TECNAI G2 transmission electron microscope. The spectroscopic characteristics of the samples were investigated using Raman spectroscopy (HORIBA, LabRAM HR Evolution) with a laser wavelength of 532 nm, Fourier transform infrared spectroscopy (Bruker TENSOR Π), and X-ray photoelectron spectroscopy (XPS; PHI 1600 ESCA, PerkinElmer). The particle-size distributions of the samples were investigated using a dynamic light scattering instrument (ZEN3700, Malvern, UK). Thermogravimetric analysis (TGA) was performed using a TG/DTA STA449C thermal analyzer in an airflow at a heating rate of 10°C min^{-1} from the ambient temperature to 800°C.

Electrochemical measurements and computational details

The working electrode was prepared by mixing the PbSe@CNTs composite, conductive carbon (Super P), and a poly(vinyl difluoride) binder at a weight ratio of 8:1:1 with *N*-methyl-2-pyrrolidone (as a solvent) and then pasting the mixture onto Al foil, followed by drying at 70°C in a vacuum oven for 24 h. Then, the electrode was cut into small pieces (diameter of 12 mm) with mass loading of 2.4 mg cm^{-2}. CR2032-type coin cells were assembled with the prepared working electrode, pure Na foil (12 mm in diameter) as the counter electrode, porous glass fiber as the separator, and 1 mol L^{-1} $NaPF_6$ dissolved in dimethoxyethane as the electrolyte in an Ar-filled glovebox (<0.01 ppm O_2 and <0.01 ppm H_2O, Universal, MIKROUNA) and used to evaluate the electrochemical performance of the PbSe@CNTs electrodes. Galvanostatic tests were performed in the voltage range of 0.01–3.0 V (*vs*. Na^+/Na) using a LAND battery tester (CT3001A). Cyclic voltammetry (CV) measurements and electrochemical impedance spectroscopy (EIS) were performed on a CHI 760E electrochemical workstation. For the galvanostatic intermittent titration technique (GITT) measurements, the cells were discharged at 50 mA g^{-1} for 30 min, followed by a relaxation process under the open-circuit potential for 2 h. For comparison, PbSe, Super P, and CNTs electrodes were prepared and tested in the same manner. All the electrochemical measurements were performed at room temperature.

Density functional theory (DFT) calculations were performed using the Vienna *Ab initio* simulation package [39]. The interaction between electrons and ions was demonstrated by the projector augmented wave pseudopotential with a cutoff energy of 450 eV [40]. The electronic exchange-correlation effect was described by the generalized gradient approximation with the Perdew-Burke-Ernzerhof function [41]. The convergence criteria of energy and force were set to 10^{-5} eV and 0.02 eV Å^{-1}, respectively.

RESULTS AND DISCUSSION

The PbSe@CNTs were prepared *via* a high-energy ball-milling method, and the detailed synthesis mechanism is presented in Fig. S1. The recovered Pb and Se powders reacted and bonded with each other to form a new phase PbSe under the high-energy ball milling, during which the CNTs uniformly hinged the PbSe nanoparticle. The chemical components and crystal phases of the pristine and obtained products were determined *via* XRD analysis, Raman spectroscopy, and XPS. Fig. 1a and Fig. S2 present the XRD patterns of PbSe@CNTs, PbSe, CNTs, Pb, and Se. As shown, the synthesized PbSe and PbSe@CNTs peaks matched the cubic *Fm*-3*m* space group PbSe, and the pattern differed significantly from those for pristine Se and Pb (Fig. S2), indicating the high purity and crystallinity of the as-prepared samples [35]. The crystallinity of the PbSe@CNTs was reduced after the introduction of CNTs (compared with that of the pure PbSe), and the widened peak is attributed to the reduction of PbSe grains and their isolation due to the addition of CNTs. In the high-resolution TEM (HRTEM) image in the inset of Fig. 1a, well-developed lattices with *d*-spacings of 0.217 and 0.305 nm of a PbSe nanoparticle are observed, which correspond to the (220) and (200) facets. Furthermore, the angle between the two facets was measured to be approximately 45°, which is consistent with cubic PbSe. The Raman spectra were used to explain the chemical-shift change of Pb and Se, as shown in Fig. 1b and Fig. S3. The Raman spectrum of the PbSe@CNTs differed significantly from those of Se and Pb (Fig. S3). A strong resonance peak at 136.5 cm^{-1} was observed, corresponding to the first-order resonant optical phonon (LO) of PbSe, along with a peak at 273.6 cm^{-1} related to the double-phonon scattering of PbSe [42]. The sp mode of PbSe caused the resonance peak at 83 cm^{-1}. Two characteristic bands of C (amorphous (D) and graphitic (G) bands located at 1400 and 1600 cm^{-1}) were observed for the PbSe@CNTs samples, suggesting the existence of CNTs [12]. The PbSe@CNTs exhibited the same vibration mode as PbSe, indicating that the introduction of CNTs did not change the structure or composition of PbSe.

Fig. 1c presents the XPS spectra of Pb 4f for PbSe and

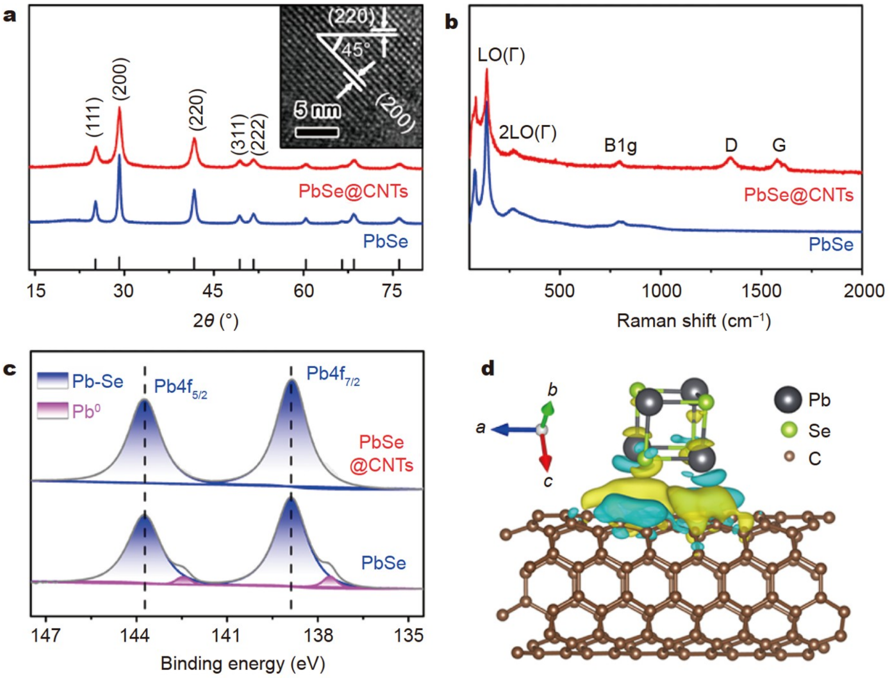

Figure 1 Characterization of PbSe@CNTs and PbSe. (a) XRD patterns with an HRTEM image (inset), (b) Raman spectra, and (c) Pb 4f XPS spectra of PbSe@CNTs and PbSe samples; (d) PbSe binding with CNTs and the simulated charge distribution between the CNTs and PbSe. The cyan and yellow areas indicate a decrease and increase in the electron density, respectively.

PbSe@CNTs. As shown, Pb completely and uniformly bonded with Se after the addition of CNTs. PbSe without CNTs exhibited a few Pb metal peaks, due to unreacted Pb, indicating that the introduced CNTs promoted the formation of the PbSe phase. The peak at 291 eV of the C 1s XPS spectrum in Fig. S4 indicates the formation of a chemical bond between PbSe and CNTs, which enhances the electron transport. The CNTs encompassed and segregated PbSe nanoparticles, suppressing their aggregation and increasing the electronic conductivity. Furthermore, the interaction between PbSe and CNTs was indicated by the differential charge density based on DFT calculations, as shown in Fig. 1d. The adsorption of PbSe caused the electrons around CNTs to be accumulated or depleted. The redistributed charge matched the positive charge of Pb and the negative charge of Se, strengthening the electrostatic interaction. Consequently, the intrinsic conductivity of the PbSe@CNTs (0.151 S m^{-1}) was higher than that of PbSe (0.045 S m^{-1}), as indicated by the current-voltage (*I*-*V*) curves in Fig. S5 [14]. The CNT content in the PbSe@CNTs composites can be determined *via* TGA. The mass loading of the CNTs in the PbSe@CNTs composites was estimated to be ~9.8%, as shown in Fig. S6. The presence of well-surrounded CNTs between PbSe nanoparticles can be useful in electrochemical applications to facilitate electron conduction, buffer large volume changes, restrain the aggregation of discharged products, and maintain the integrity of electrodes during the sodiation/desodiation process.

The morphologies and microstructures of the samples were characterized *via* SEM and TEM. As shown in Fig. 2a, b, irregular nanoparticles agglomerated as clusters containing hundreds of individual crystallites surrounded by CNTs were observed in the PbSe@CNTs. PbSe nanoparticles twined and wound by CNTs were clearly observed in the TEM images (Fig. 2c and Fig. S7). PbSe without CNTs (Figs S8a and S9) had a smooth surface and a larger particle size. Compared with PbSe, the particle size of the PbSe@CNTs was smaller according to the SEM and TEM results. In addition, the CNTs inhibited the agglomeration of PbSe nanoparticles, and the TEM images confirmed the bridging chain structure of the composites (Fig. 2c), whereas the PbSe exhibited a granular shape with separate particles. It may be reasonably asserted that the CNTs reduced the particle size of PbSe and suppressed the aggregation of PbSe particles. Furthermore, the particle sizes of the PbSe@CNTs and PbSe were determined *via* dynamic light scattering (DLS), as shown in Fig. 2d and Fig. S8b, respectively. The results indicate that the hydrodynamic diameter of the PbSe@CNTs was approximately 91.2 nm, which was consistent with the SEM results and the average particle size of 104 nm estimated from the XRD peaks of Fig. 1a using the Scherrer equation [12]. The average particle size of pure PbSe was determined to be 220 nm, which was larger than that of the composite with CNTs. This suggests that the CNTs inhibited the aggregation of PbSe nanoparticles and separated the nanocrystals. This bridging chain structure resulted from the nucleation and growth of PbSe crystals between CNTs and PbSe crystals during the synthesis process. The uniform composite had good electrical contact between PbSe particles and CNTs, which prevented the pulverization of PbSe particles during the cycling process, ensuring a good electrochemical performance.

The electrochemical properties of PbSe@CNTs and pure PbSe were studied in coin cells *via* different electrochemical analysis techniques. Fig. 3a shows the typical CV curves of the PbSe@CNTs electrode over the first three cycles from 0.01 to 3.0 V at 0.1 mV s^{-1}. Five pairs of redox peaks are observed, which are well overlapped, suggesting the highly reversible sodiation/desodiation of PbSe@CNTs. The reduction peaks in the cathodic scans (0.034, 0.094, 0.201, 0.446, and 1.007 V)

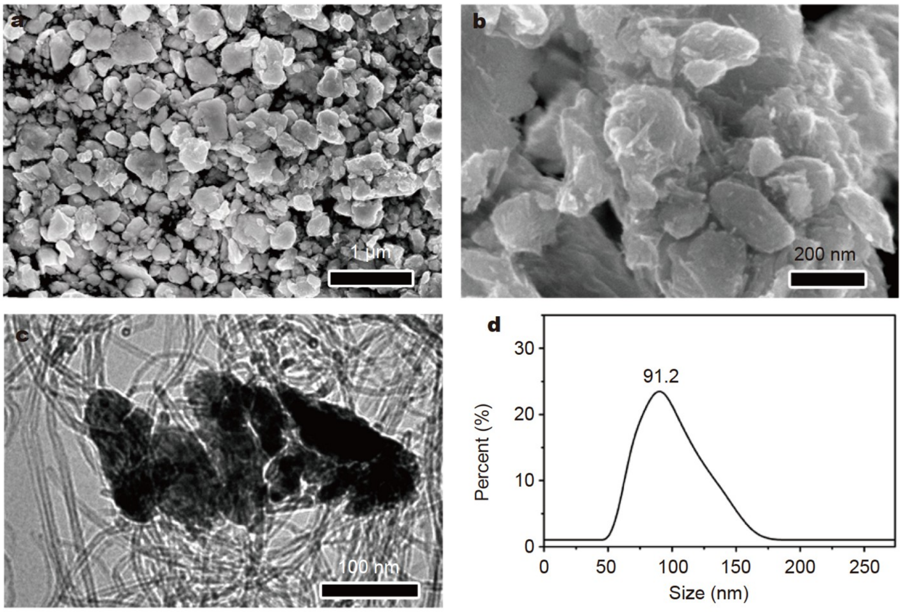

Figure 2 Morphology characterization: (a, b) SEM and (c) TEM images of PbSe@CNTs samples; (d) particle-size distribution of PbSe@CNTs powders obtained *via* DLS.

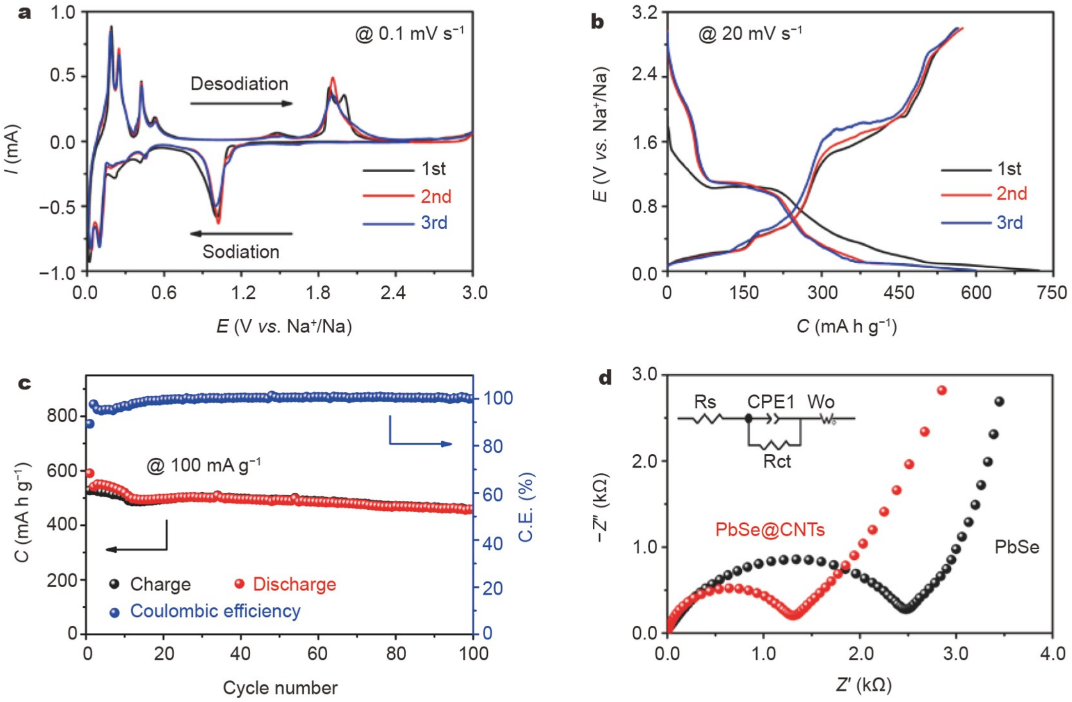

Figure 3 Electrochemical properties of the PbSe@CNTs electrode in SIBs: (a) CV curves of the PbSe@CNTs electrode at 0.1 mV s^{-1} between 0.01 and 3.0 V; (b) charge/discharge curves at 20 mA g^{-1}; (c) long-cycling performance at 100 mA g^{-1}; (d) EIS results for the PbSe@CNTs and PbSe electrodes in SIBs.

correspond to the Na embeding reaction of the material, indicating that there were two main step reactions for Na_2Se and $Na_{15}Pb_4$. The second step involved four alloying reactions for the formation of $NaPb_3$, NaPb, Na_9Pb_4, and $Na_{15}Pb_4$, respectively. The following oxidation peaks (0.184, 0.248, 0.428, 0.534, and 1.909 V) are attributed to the gradual desodiation of the Na-Pb alloy and Na_2Se to reform PbSe, indicating good reversibility. The first three galvanostatic charge/discharge curves of the PbSe@CNTs electrode at 20 mA g^{-1} are shown in Fig. 3b. Two slope plateaus in the charge/discharge process are attributed to the sodiation/desodiation of Se and Pb active sites, respectively, consistent with the CV curves in Fig. 3a. The electrode delivered an initial discharge capacity of 722.7 mA h g^{-1} in the first cycle and a reversible charge capacity of 597 mA h g^{-1}. The low Coulombic efficiency in the first cycle was due to the formation of a solid-electrolyte interface film and the irreversible capacity of the conductive C (Super P) and CNTs (Fig. S10). The overlapped CV and charge/discharge curves in the initial three cycles indicate that the sodiation/desodiation process of the PbSe@CNTs was more stable and reversible than that of PbSe (Fig. S11). The rate performance of the PbSe@CNTs electrode at different current densities ranging from 10 to 500 mA g^{-1} is presented in Fig. S12. The electrode delivered reversible capacities of 598, 570.8, 562.3, 475.7, 450.2, and 416.4 mA h g^{-1} at 10, 20, 50, 100, 200, and 500 mA g^{-1}, respectively. There was no obvious dissolution in the disassembled cell after 10 cycles (Fig. S13), indicating that the polyselenide diffusion was significantly suppressed through the bonding of Pb and Se.

Furthermore, a high reversible capacity of 458.9 mA h g^{-1} at 100 mA g^{-1} remained after 100 cycles with a Coulombic efficiency of 100%, corresponding to a capacity retention of 88%, as shown in Fig. 3c. The PbSe@CNTs sample had better electrochemical performance than previously reported Se/Pb-based anodes regarding to the reversible capacity and potential, as indicated by Table S1. To further quantify the role of the introduced CNTs, EIS measurements were conducted on PbSe@CNTs and pure PbSe. As shown in Fig. 3d, the PbSe@CNTs electrode exhibited a smaller semicircle in the mid-frequency zone than the pristine PbSe. According to the fitting circuit model shown in Fig. 3d (inset), the fitting radius was almost two times smaller, and the electron-transfer resistances of the two samples were 1222 and 2588 Ω, respectively. The smaller electron-transfer resistance (R_{ct}) and interfacial resistance (R_{s}) of the PbSe@CNTs were mainly due to the high conductivity of the CNTs (Fig. S5) and the modified grain size and structure, which facilitated the penetration of the electrolyte (Fig. S14). Additionally, a full SIB consisting of a PbSe@CNTs anode and a $\mathrm{Na_3V_2(PO_4)_3}$ cathode was assembled, as schematically shown in Fig. S15a. The full battery exhibited multiple charge/discharge platforms with a discharge capacity of 440 mA h g^{-1} (based on the mass of the negative electrode), which are consistent with the voltage curves matched by the positive and negative electrodes in Fig. S15b. A discharge capacity of 361 mA h g^{-1} at 50 mA g^{-1} was remained after 30 cycles (Fig. S15c). As a demonstration, two light-emitting diodes were powered by a full coin cell, as shown in Fig. S15d. These results indicate the application potential of the PbSe@CNTs anode for SIBs.

To clarify the kinetics of the Na-storage behavior in the PbSe@CNTs electrode, we analyzed the CV responses of the PbSe@CNTs electrode at different scan rates ranging from 0.2 to 0.8 mV s^{-1}, as shown in Fig. 4a. In all cases, four pairs of reduction peaks (R1, R2, R3, and R4) and oxidation peaks (O1, O2, O3, and O4) were observed. The relationship between the peak current (i) and the scan rate (v) can be described as $i = av^b$, where a and b are positive variables. In general, the contribution of pseudocapacitance is reflected by the value of the coefficient b. When b = 0.5, the electrochemical process is controlled by ion diffusion. When b = 1, it is mainly affected by pseudocapacitance. The peak currents increase with an increasing scan rate primarily according to the square-root dependence of the Randles-Sevcik equation for solution-to-interface diffusion [12,34]. The b values of the CV peaks of the PbSe@CNTs electrode were close to 0.5, except for the R2 and R3 peaks, as indicated by the linear-fitting results in Fig. 4b, indicating that the charge/discharge process was Faradaic depended diffusion of Na$^+$. The peak currents (i) of Fig. 4a are plotted against the square roots of the scan rates (v) in Fig. S16, according to the Randles-Sevcik equation [43]. Accordingly, the diffusion coefficients (D_{Na^+}) for each oxidation and reduction step were calculated to be approximately 10^{-14}–10^{-13} cm^2 s^{-1}, exhibiting large values for the electrolyte phase, which ensured the good rate performance of the charge/discharge steps in the PbSe@CNTs electrode. Moreover, the Na$^+$ transport in the PbSe@CNTs electrode was investigated using the GITT, as shown in Fig. 4c [44]. Typically, the chemical diffusion coefficient can be calculated using the equation $D_{\mathrm{Na}^+} = 4/\pi t(m_{\mathrm{B}}V_{\mathrm{M}}/M_{\mathrm{B}}S)^2(\Delta E_{\mathrm{s}}/\Delta E_{\mathrm{t}})^2$, where t is the

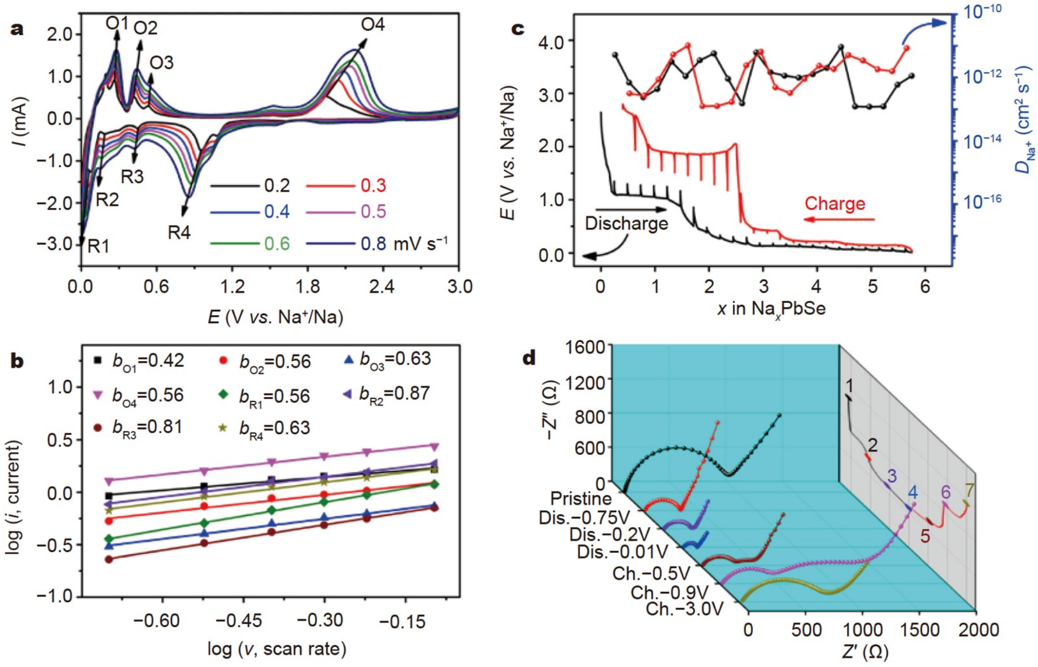

Figure 4 Reaction kinetics of the PbSe@CNTs electrode: (a) CV curves for different scan rates; (b) the corresponding log$i$ vs. log$v$ plots for different redox states; (c) GITT curves and the corresponding calculated diffusion coefficients for the charge/discharge process; (d) EIS spectra for different states in the sodiation/desodiation processes.

pulse duration, m_B and M_B are the mass and molecular weight, V_M is the molar volume, S is the active surface area of the electrode, ΔE_s is the change in the steady-state voltage, and ΔE_t is the variation of cell voltage during the time period [45]. The diffusion coefficient (D_{Na^+}) of Na^+ in the insertion process was calculated by analyzing the GITT results. According to Fick's second law, the value of D_{Na^+} was calculated as 9.84×10^{-13}–1.01×10^{-11} cm^2 s^{-1} for the whole process of Na^+ embedding/desorption, which was slightly higher than that calculated from the CV results. Fast solution-phase Na^+ transport was ensured by the nanosized particles and good electrolyte wettability. The large diffusion coefficients account for the good rate performance.

The conductivity of the electrode during the charge/discharge process was measured using staircase potentiostatic EIS, as shown in Fig. 4d and Table S2. R_{ct} decreased with the Na^+ intercalation from point 1 to point 4 and then increased with the Na^+ extraction from point 4 to point 7. Simultaneously, the slope of the straight line in the low-frequency region of the EIS curve increased with the Na^+ intercalation from point 1 to point 4, indicating that the Na^+ diffusion was enhanced during the Na^+ intercalation process. The reduced R_{ct} and enhanced Na^+ diffusion are attributed to the formation of an intermediate phase, i.e., metallic Pb and Na_xPb alloys, during the discharge process. Correspondingly, the slope of the straight line decreased with the Na^+ extraction from point 4 to point 7, indicating that the Na^+ diffusion slowed in the Na^+ extraction process.

To comprehensively investigate the mechanism of Na storage in the PbSe@CNTs electrode, *ex situ* XRD and Raman tests were performed during the first cycle. Fig. 5a presents the typical charge/discharge curves of the PbSe@CNTs electrode at 50 mA g^{-1} (a, b, c, d, e, f, g, and h present selected discharged and charged states: original, discharge to 0.75/0.15/0.05 V, fully discharged, charge to 0.3/1.2 V, and fully charged, respectively). Fig. 5b shows the corresponding *ex situ* XRD patterns obtained during the charge/discharge process. The pristine PbSe@CNTs electrode (state a) exhibited obvious diffraction peaks at 25.2°, 29.1°, 41.7°, 49.3°, and 51.7°. The diffraction peak at 65.1° was assigned to the current collector. With discharge to 0.75 V (state b), the diffraction peaks of PbSe disappeared. New diffraction peaks of Na_2Se (22.6° and 37.2°) and Pb (31.3°, 36.3°, 50.2°, and 63°) appeared. In the state c (discharged to 0.15 V), several new diffraction peaks corresponding to a cubic phase of NaPb were observed [33]. With discharge to 0.05 V (state d), the characteristic diffraction peaks of Na_9Pb_4 were evident. After the electrode was fully discharged to 0.01 V (state e), diffraction peaks were observed at 16.58°, 19.08°, 31.88°, 33.38°, 34.78°, and 37.48°, indicating that the final discharge product was cubic $Na_{15}Pb_4$. In the reverse process, $Na_{15}Pb_4$ was gradually desodiated to $NaPb_3$ (state f) and then to Pb (state g). Finally, the crystal phase was restored to the original state of PbSe in the state h (fully charged to 3.0 V). According to the XRD results, Na_2Se and $Na_{15}Pb_4$ were generated when the discharge process was complete, and they were reversibly converted into PbSe after being fully charged. In addition, no diffraction peaks of polyselenides appeared during the charge/discharge process. The dual conversion-alloying Na-storage mechanism of PbSe ensures a high theoretical capacity.

This reaction process was confirmed by *ex situ* Raman spectroscopy, as shown in Fig. 5c. The original PbSe material exhibited four vibration absorption peaks located at 83, 136.5, 273.6, and 791.7 cm^{-1} (state a). With discharge to 0.75 V (state b), sharp peaks corresponding to the vibration of Pb–Pb in Pb metal appeared at 82 and 137 cm^{-1}. Additionally, a new broad peak appeared at 271 cm^{-1}, which is attributed to the superposition of Na_2Se and Pb–Pb vibration peaks [46]. After the electrode was fully discharged to 0.01 V (state e), only the stretching vibration peak of Na_2Se at 251 cm^{-1} was retained, and

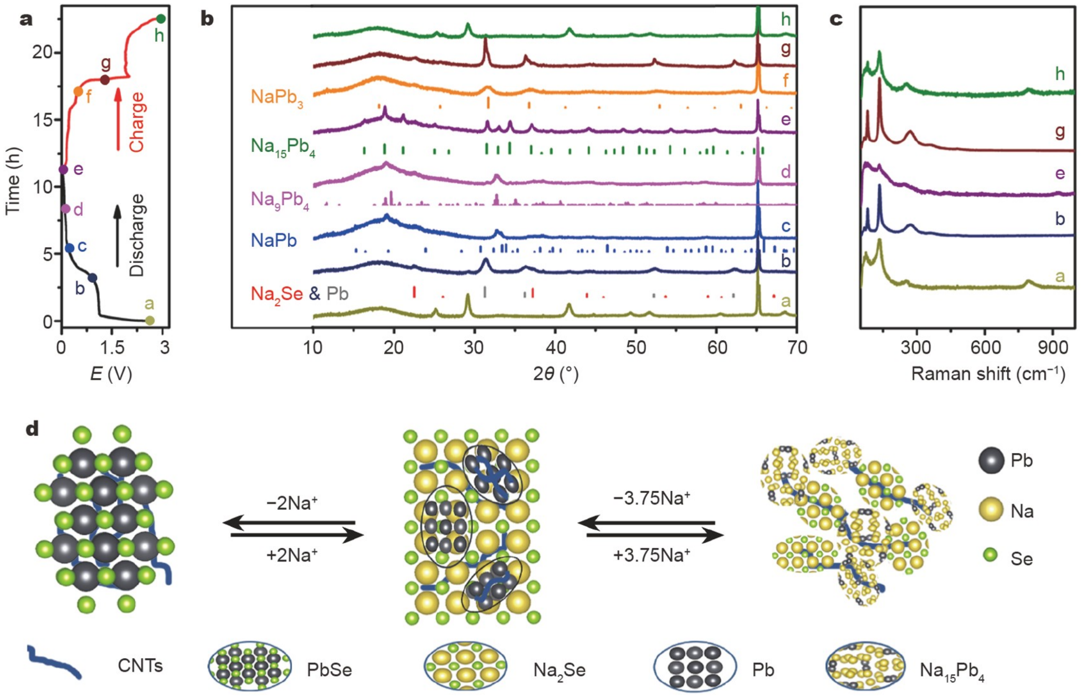

Figure 5 Na storage mechanism of PbSe: (a) the charge/discharge curve of the PbSe@CNTs electrode; (b) *ex situ* XRD patterns; (c) *ex situ* Raman spectra of the PbSe@CNTs electrode in the charge/discharge process; (d) schematic illustration of the dual conversion-alloying mechanism of PbSe@CNTs.

other peaks weakened due to the discharged product $Na_{15}Pb_4$. During the charging process, sharp peaks caused by the Pb–Pb bond were regenerated in state g (charged to 1.2 V). When the charging process was complete, the characteristic peaks of PbSe@CNTs were observed, and no impurity peaks of other products existed, which is consistent with the XRD results in Fig. 5b. There was no formation of polyselenides in the charge/discharge process, and the high reversibility of the PbSe@CNTs was confirmed by the long cycling stability.

According to the foregoing analysis, the discharge process of PbSe@CNTs can be divided into two main steps, as shown in Fig. 5d. Generally, step 1 is the formation of Na_2Se and Pb metal, and step 2 is the alloying process of Pb-Na alloys, which involves four alloying phases of $NaPb_3$, NaPb, Na_9Pb_4, and $Na_{15}Pb_4$. The charging process is highly reversible. Therefore, the reaction mechanism of the PbSe@CNTs material can be described by the following formulas:

Step 1: $PbSe + 2Na^+ + 2e^- \leftrightarrow Pb + Na_2Se$.

Step 2: $Pb + 3.75Na^+ + 3.75e^- \leftrightarrow 0.25Na_{15}Pb_4$.

Total reaction: $PbSe + 5.75Na^+ + 5.75e^- \leftrightarrow 0.25Na_{15}Pb_4 + Na_2Se$.

According to the formulas, PbSe can accommodate 5.75 Na^+, and its theoretical specific capacity is ~538.7 $mA\ h\ g^{-1}$. The bonding between Se and the active metal Pb fundamentally inhibits the formation of polyselenides and solves the dissolution problem of polyselenides. In the first stage of the discharge process, Na_2Se and Pb quasicrystals are formed. The connection between Pb atoms and CNTs forms electronic channels, providing a bridge for the internal reaction of the battery, which connects Na_2Se particles. Thus, the electrical conductivity of the material is increased, and the aggregation of Na_2Se particles is limited, as confirmed by the reduced impedance in Fig. 4d. Additionally, owing to their good conductivity, the Na_2Se particles provide a medium for the reaction of Pb and Na ions. The PbSe, Na_2Se, and Pb with a similar face-centered cubic structure are conducive to the reaction. In short, the redox potentials of Na_2Se and $Na_{15}Pb_4$ are different and the initial formation of Pb limits the growth and aggregation of Na_2Se particles. Meanwhile, Na_2Se nanoparticles can be used as conductive channel and shielding matrix to promote the Pb-Na alloying reaction. This synergistic Na-storage process allows the PbSe electrode to withstand volume changes and maintain its structural integrity during sodiation/desodiation.

CONCLUSIONS

A PbSe@CNTs nanocomposite was prepared *via* a simple mechanical ball-milling method and used as an anode material for SIBs. The structural stability and phase evolution during cycling were explained by *ex situ* XRD and Raman spectroscopy. Owing to the cooperation of the active metal Pb and Se, the formation of polyselenide was inhibited significantly. Well-surrounded and connected CNTs increased the electronic conductivity of the PbSe nanoparticles, which facilitated the electrolyte penetration into the electrode and relieved the volume expansion of PbSe nanoparticles. Therefore, the PbSe@CNTs nanocomposite exhibited excellent electrochemical properties, showing a capacity of 597 $mA\ h\ g^{-1}$ at 20 $mA\ g^{-1}$ and a capacity retention of 88% for 100 cycles at 100 $mA\ g^{-1}$. The kinetics of the PbSe@CNTs electrode in SIBs were analyzed *via* CV and GITT, and it was confirmed that the high conductivity of the CNTs and the strong bonding between CNTs and PbSe were the main reasons for fast Na^+ diffusion. These results indicate that PbSe@CNTs nanocomposites have considerable potential as the anode materials for SIBs and provide guidance for the development of dual conversion-alloying anode materials.

Received 7 April 2022; accepted 19 May 2022;

1 Vaalma C, Buchholz D, Weil M, *et al.* A cost and resource analysis of sodium-ion batteries. Nat Rev Mater, 2018, 3: 18013

2 Hirsh HS, Li Y, Tan DHS, *et al.* Sodium-ion batteries paving the way for grid energy storage. Adv Energy Mater, 2020, 10: 2001274

3 Abraham KM. How comparable are sodium-ion batteries to lithium-ion counterparts? ACS Energy Lett, 2020, 5: 3544–3547

4 Zhu YF, Xiao Y, Dou SX, *et al.* Spinel/post-spinel engineering on layered oxide cathodes for sodium-ion batteries. eScience, 2021, 1: 13–27

5 Wang L, Ni Y, Lei K, *et al.* 3D porous tin created by tuning the redox potential acts as an advanced electrode for sodium-ion batteries. ChemSusChem, 2018, 11: 3376–3381

6 Stevens DA, Dahn JR. The mechanisms of lithium and sodium insertion in carbon materials. J Electrochem Soc, 2001, 148: A803

7 Wen Y, He K, Zhu Y, *et al.* Expanded graphite as superior anode for sodium-ion batteries. Nat Commun, 2014, 5: 4033

8 Zhu Z, Cheng F, Hu Z, *et al.* Highly stable and ultrafast electrode reaction of graphite for sodium ion batteries. J Power Sources, 2015, 293: 626–634

9 Jache B, Adelhelm P. Use of graphite as a highly reversible electrode with superior cycle life for sodium-ion batteries by making use of co-intercalation phenomena. Angew Chem Int Ed, 2014, 53: 10169–10173

10 Perveen T, Siddiq M, Shahzad N, *et al.* Prospects in anode materials for sodium ion batteries—A review. Renew Sustain Energy Rev, 2020, 119: 109549

11 Ren M, Fang H, Wang C, *et al.* Advances on manganese-oxide-based cathodes for Na-ion batteries. Energy Fuels, 2020, 34: 13412–13426

12 Wang L, Voskanyan AA, Chan KY, *et al.* Combustion synthesized porous bismuth/N-doped carbon nanocomposite for reversible sodiation in a sodium-ion battery. ACS Appl Energy Mater, 2020, 3: 565–572

13 Tan H, Feng Y, Rui X, *et al.* Metal chalcogenides: Paving the way for high-performance sodium/potassium-ion batteries. Small Methods, 2020, 4: 1900563

14 Wang L, Ni Y, Hou X, *et al.* A two-dimensional metal-organic polymer enabled by robust nickel-nitrogen and hydrogen bonds for exceptional sodium-ion storage. Angew Chem Int Ed, 2020, 59: 22126–22131

15 Yang Z, Zhu K, Dong Z, *et al.* Stabilization of Li-Se batteries by wearing PAN protective clothing. ACS Appl Mater Interfaces, 2019, 11: 40069–40077

16 Luo M, Yu H, Hu F, *et al.* Metal selenides for high performance sodium ion batteries. Chem Eng J, 2020, 380: 122557

17 Chen H, Mu Z, Li Y, *et al.* $SnSe_2$ nanocrystals coupled with hierarchical porous carbon microspheres for long-life sodium ion battery anode. Sci China Mater, 2020, 63: 483–491

18 Zhang K, Park M, Zhou L, *et al.* Urchin-like $CoSe_2$ as a high-performance anode material for sodium-ion batteries. Adv Funct Mater, 2016, 26: 6728–6735

19 Xie L, Yang Z, Sun J, *et al.* Bi_2Se_3/C nanocomposite as a new sodium-ion battery anode material. Nano-Micro Lett, 2018, 10: 50

20 Wang T, Yang K, Shi J, *et al.* Simple synthesis of sandwich-like $SnSe_2$/rGO as high initial Coulombic efficiency and high stability anode for sodium-ion batteries. J Energy Chem, 2020, 46: 71–77

21 Song J, Qiu S, Hu F, *et al.* Sub-2 nm thiophosphate nanosheets with heteroatom doping for enhanced oxygen electrocatalysis. Adv Funct Mater, 2021, 31: 2100618

22 Wu J, Ihsan-Ul-Haq M, Ciucci F, *et al.* Rationally designed nanostructured metal chalcogenides for advanced sodium-ion batteries. Energy Storage Mater, 2021, 34: 582–628

23 Deng W, Chen J, Yang L, *et al.* Solid solution metal chalcogenides for

sodium-ion batteries: The recent advances as anodes. Small, 2021, 17: 2101058
24 Zheng R, Yu H, Zhang X, *et al.* A $TiSe_2$-graphite dual ion battery: Fast Na-ion insertion and excellent stability. Angew Chem, 2021, 133: 18578–18585
25 Xiao Y, Zhao X, Wang X, *et al.* A nanosheet array of Cu_2Se intercalation compound with expanded interlayer space for sodium ion storage. Adv Energy Mater, 2020, 10: 2000666
26 Tang C, Wei X, Cai X, *et al.* ZnSe microsphere/multiwalled carbon nanotube composites as high-rate and long-life anodes for sodium-ion batteries. ACS Appl Mater Interfaces, 2018, 10: 19626–19632
27 Ali Z, Zhang T, Asif M, *et al.* Transition metal chalcogenide anodes for sodium storage. Mater Today, 2020, 35: 131–167
28 Kong F, Han Z, Tao S, *et al.* Core-shell structured SnSe@C microrod for Na-ion battery anode. J Energy Chem, 2021, 55: 256–264
29 Wang L, Wang C, Zhang N, *et al.* High anode performance of *in situ* formed Cu_2Sb nanoparticles integrated on Cu foil *via* replacement reaction for sodium-ion batteries. ACS Energy Lett, 2017, 2: 256–262
30 Deng L, Hu F, Ma M, *et al.* Electronic modulation caused by interfacial Ni–O–M (M = Ru, Ir, Pd) bonding for accelerating hydrogen evolution kinetics. Angew Chem Int Ed, 2021, 60: 22276–22282
31 Peng S, Han X, Li L, *et al.* Electronic and defective engineering of electrospun $CaMnO_3$ nanotubes for enhanced oxygen electrocatalysis in rechargeable zinc-air batteries. Adv Energy Mater, 2018, 8: 1800612
32 Fang L, Bahlawane N, Sun W, *et al.* Conversion-alloying anode materials for sodium ion batteries. Small, 2021, 17: 2101137
33 Darwiche A, Dugas R, Fraisse B, *et al.* Reinstating lead for high-loaded efficient negative electrode for rechargeable sodium-ion battery. J Power Sources, 2016, 304: 1–8
34 Li M, Yang J, Liang S, *et al.* Review on clean recovery of discarded/spent lead-acid battery and trends of recycled products. J Power Sources, 2019, 436: 226853
35 Lu T, Zhao J, Yuan J, *et al.* PbSe/sulfur-doped carbon nanocube composites prepared from Pb-MOF precursors as anode materials for lithium and sodium-ion batteries. J Alloys Compd, 2021, 874: 159942
36 Li L, Yu D, Li P, *et al.* Interfacial electronic coupling of ultrathin transition-metal hydroxide nanosheets with layered MXenes as a new prototype for platinum-like hydrogen evolution. Energy Environ Sci, 2021, 14: 6419–6427
37 Huang H, Yu D, Hu F, *et al.* Clusters induced electron redistribution to tune oxygen reduction activity of transition metal single-atom for metal-air batteries. Angew Chem Int Ed, 2022, 61: e202116068
38 Zhao D, Wang L, Qiu M, *et al.* Amorphous Se restrained by biomass-derived defective carbon for stable Na-Se batteries. ACS Appl Energy Mater, 2021, 4: 7219–7225
39 Ni Y, Lin L, Shang Y, *et al.* Regulating electrocatalytic oxygen reduction activity of a metal coordination polymer *via* d-π conjugation. Angew Chem, 2021, 133: 17074–17078
40 Blöchl PE. Projector augmented-wave method. Phys Rev B, 1994, 50: 17953–17979
41 Perdew JP, Burke K, Ernzerhof M. Generalized gradient approximation made simple. Phys Rev Lett, 1996, 77: 3865–3868
42 Habinshuti J, Kilian O, Cristini-Robbe O, *et al.* Anomalous quantum confinement of the longitudinal optical phonon mode in PbSe quantum dots. Phys Rev B, 2013, 88: 115313
43 Wang L, Wang C, Li F, *et al.* *In situ* synthesis of Bi nanoflakes on Ni foam for sodium-ion batteries. Chem Commun, 2018, 54: 38–41
44 Leftheriotis G, Papaefthimiou S, Yianoulis P. Dependence of the estimated diffusion coefficient of Li_xWO_3 films on the scan rate of cyclic voltammetry experiments. Solid State Ion, 2007, 178: 259–263
45 Jian Z, Yu H, Zhou H. Designing high-capacity cathode materials for sodium-ion batteries. Electrochem Commun, 2013, 34: 215–218
46 Lu Y, Zhou P, Lei K, *et al.* Selenium phosphide (Se_4P_4) as a new and promising anode material for sodium-ion batteries. Adv Energy Mater, 2017, 7: 1601973

Acknowledgements This work was supported by the National Natural Science Foundation of China (22109037), the Natural Science Foundation of Hebei Province (B2020201001), the Advanced Talents Incubation Program of Hebei University (521000981408), the Young Elite Scientists Sponsorship Program by CAST (2021QNRC001), and the Research Innovation Team of the College of Chemistry and Environmental Science of Hebei University (hxkytd2102). Wang L thanks NaXun Energy Technology Co., LTD (China) for the technical support.

Author contributions Wang L proposed the concept. Wang L and Zhang N supervised the work; Zhao D, Zhao X, and Liu N carried out the experiments, characterizations, and electrochemical measurements; Zhao D and Wang L wrote the manuscript; Qin B, Qiu M, and Zhang N helped to discuss and analyze the data. All authors contributed to the general discussion.

Conflict of interest The authors declare that they have no conflict of interest.

Supplementary information Supporting data are available in the online version of the paper.

Dongdong Zhao received her BSc degree from Tangshan Normal University. She is currently a master student at Hebei University. Her research interests mainly focus on high-performance electrode materials for sodium-ion batteries.

Ning Zhang received his BSc degree from Hebei University in 2012 and then obtained his PhD degree in inorganic chemistry from Nankai University in 2017. He is now a professor at the College of Chemistry & Environmental Science, Hebei University. His current research focuses on the design and synthesis of functional materials for applications in energy storage and conversion (lithium/sodium-ion batteries and aqueous zinc batteries).

Liubin Wang received his BE degree in materials science and engineering from Southwest Jiaotong University and PhD degree in physical chemistry from Nankai University. He worked as a visiting student at The University of Hong Kong in 2019. He joined Hebei University as a professor in 2020. His research interests focus on the design of electrodes and electrolytes for high-energy electrochemical devices, including metal-ion batteries, aqueous batteries, and photo-assisted rechargeable batteries.

基于转化-合金化机制的钠离子电池PbSe@CNTs负极材料

赵东东[1], 张宁[1*], 赵小莹[1], 刘宁博[1], 覃彬[2], 仇满德[1], 王刘彬[1*]

摘要 钠离子电池作为新型的储能电池体系因钠资源储量丰富、成本低廉等优势有望填补锂离子电池在某些应用领域的空缺，非常适用于大规模储能领域．然而，高容量储钠负极材料仍然需要进一步研究．本文以废旧铅酸电池的回收铅和商业化硒粉为原料，采用机械球磨法制备了纳米硒化铅与碳纳米管(PbSe@CNTs)的复合材料．碳纳米管网络缠绕在PbSe纳米粒子上，可有效抑制纳米粒子的团聚，同时提高了电子导电性．纳米级的PbSe和拓扑结构的CNTs有利于电解液的渗透，缩短了Na^+和电子的传输路径，缓解了脱嵌钠过程中的机械应变，提高了倍率和长循环稳定性能．PbSe@CNTs电极在20 mA g^{-1}电流密度下具有597 mA h g^{-1}的可逆比容量，在100 mA g^{-1}循环100圈仍保持458.9 mA h g^{-1}的可逆比容量，容量保持率为88%．通过X射线衍射和拉曼光谱分析，证实了PbSe的储钠机理为两步转化-合金化过程，反应方程式为$PbSe + 5.75Na^+ + 5.75e^- \leftrightarrow 0.25Na_{15}Pb_4 + Na_2Se$.